Engineering Fracture Mechanics 239 (2020) 107274

Contents lists available at ScienceDirect

Engineering Fracture Mechanics

journal homepage: www.elsevier.com/locate/engfracmech

A mixed mode cohesive model for FRP laminates incorporating large scale bridging behaviour

R.K. Joki[a,b,c,*], F. Grytten[c], B. Hayman[d], B.F. Sørensen[e]

[a] FiReCo AS, Storgata 15, 1605 Fredrikstad, Norway
[b] University of Oslo, Department of Mathematics, Pb 1053 Blindern, 0316 Oslo, Norway
[c] SINTEF Industry, Department of Materials and Nanotechnology, Pb. 124 Blindern, 0314 Oslo, Norway
[d] Technical University of Denmark, Department of Mechanical Engineering, Kongens Lyngby, Denmark
[e] Technical University of Denmark, Department of Wind Energy, Frederiksborgvej 399, 4000 Roskilde, Denmark

ARTICLE INFO

Keywords:
Polymer-matrix composites (PMCs)
Delamination
Finite element analysis (FEA)
Cohesive Law (CL)

ABSTRACT

A user defined cohesive material model is implemented in the LS-DYNA finite element code. The model is based on interface properties characterised from DCB specimens loaded with unequal bending moments. Different mode mixities are obtained by applying different ratios of moments to the two beams in the cracked part of the specimen. The mixed mode cohesive law is fitted for large scale bridging delamination through inverse modelling. In this way, the variations in stress and crack opening across the width of the specimen are taken into account. The *J* integral approach is used to find a starting point for the fitting procedure. Three properties from five moment configurations are evaluated to find a first estimate of the shape of the cohesive law: crack tip fracture energy, steady-state fracture resistance and crack end-opening at steady-state fracture resistance. The parameters of the cohesive law are then further adjusted using the optimisation tool LS-OPT. The implemented cohesive model is assessed by comparing numerical to experimental test results from the standardised ASTM double cantilever beam test and the ASTM mixed mode bending test.

1. Introduction

A variety of cohesive models are available in commercial finite element codes. Often, they are characterised by initial stiffness, critical stress, fracture energy for mode I and mode II and an interpolation scheme for mixed mode delamination. Several shapes of the cohesive law have been used to model the interlaminar fracture characteristics of composites: bilinear [1–3], polynomial [4,5], exponential [6,7] and trapezoidal [8,9]. The interpolation rules can be simple linear or quadratic power laws [10] or more advanced rules such as the Benzeggagh-Kenane mode mixity rule [11]. Several studies have shown that the choice of cohesive law shape affects the results from numerical delamination models [12–15]. The standardised linear-elastic fracture mechanics (LEFM) tests for interlaminar characterisation of composite laminates give no indication of the shape of the cohesive law. A delamination test [16] where rotations (moments), rather than opening displacements (wedge forces), are applied to the beam ends of a double cantilever beam (DCB) specimen might be better suited for determining the shape of the cohesive law, since it enables cohesive laws to be determined using a *J* integral approach [17]. This can also be done by measuring the rotation of the beam where the forces are applied when delamination is promoted in DCB specimens using wedging forces [18]. However, when moments are applied rather

* Corresponding author at: FiReCo AS, Storgata 15, 1605 Fredrikstad, Norway.
E-mail addresses: Reidar.joki@fireco.no (R.K. Joki), Frode.Grytten@sintef.no (F. Grytten), bsqr@dtu.dk (B.F. Sørensen).

https://doi.org/10.1016/j.engfracmech.2020.107274
Received 13 September 2019; Received in revised form 15 April 2020; Accepted 12 August 2020
Available online 10 September 2020
0013-7944/ © 2020 The Authors. Published by Elsevier Ltd.

Nomenclature

a_0	Prefabricated crack length
B	Beam width
c	Load arm length in MMB setup
D	Damage parameter in the cohesive constitutive model.
E_{11}	Specimen Young's modulus in the longitudinal direction
H	Beam height
J_R	Fracture resistance
$J_{R,ext}$	Fracture resistance calculated from external forces
$J_{R,FPZ}$	Fracture resistance associated with the whole failure process zone
$J_{R,int}$	Fracture resistance calculated from tractions acting within fracture process zone
J_{SS}	Steady State fracture resistance
J_{tip}, J_0	Fracture resistance associated with crack-tip deformations
k_i	Cohesive stiffness
K_I, K_{II}	Stress intensity factors (mode I and mode II, respectively)
L	Length of FPZ
l	Sequence number for opening displacement in cohesive law
L_1, L_2	Load arm spacing in experimental setup
M	Moments
m	Sequence number for opening mode angle in cohesive law
n	Number of variables in optimization setup
p	Sampling points in optimization setup
P_1, P_2	Load arm loading in experimental setup
S_{22}, S_{12}	Transverse and shear stress strength, respectively, in buck material.
x_1, x_2, x_3	Orthogonal coordinate axes
Γ	Line-integral path
δ_0	Critical opening displacement
δ_n	Normal crack opening displacements
δ_t	Tangential crack opening displacements
θ	Crack opening mode angle
λ	Rate of transverse to longitudinal Young's modulus
σ^*, δ^*	* refers to crack-end properties
σ_e, δ_e	effective cohesive traction and separation, respectively.
σ_n	Normal cohesive tractions
σ_t	Tangential cohesive tractions
φ	Moment configuration
ψ	Phase angle from linear elastic fracture mechanics
Ω	Cohesive law surface

Abbreviations

ASA	Adaptive simulated annealing
CL	Cohesive Law
DCB	Double Cantilever Beam
DCB-UBM	Double Cantilever Beam loaded with unequal bending moments
FEA	Finite element analysis
FPZ	Fracture Process Zone
LEFM	Linear-elastic fracture mechanics
MMB	Mixed Mode Bending
NCF	Non-crimp fabric
UD	Unidirectional

than wedging forces, the delamination mode can be altered simply by altering the configuration of the applied moments. Equal curvature of the fracture interfaces in opposite directions promotes mode I delamination, unequal curvatures promote mixed mode delamination and equal curvature in the same direction promotes mode II delamination [19]. The fracture resistance is calculated directly from the applied moments without the need for tracking the distance from the applied load to the crack tip [17]. The fracture resistance arises from the tractions transferred between the two separating beams. The region where these tractions are transferred between the separating beams is referred to as the fracture process zone (FPZ). The path independent J integral [20] can be used to relate the calculated fracture resistance to the tractions acting in the FPZ under the assumption of plane stress or plane strain. Under mixed mode conditions, the normal and shear traction-separation relations can be calculated by partially differentiating the fracture resistance with respect to the normal end-opening and tangential end-opening displacements, respectively [21].

A three-dimensional effect that seems not to have been investigated for mixed mode cases in the published literature is the variation in the local normal opening displacement across the specimen due to anticlastic bending. This induces a variation in the values of the tractions across the FPZ in the specimen, and thus crack initiation, that needs to be accounted for before an accurate traction-separation relation can be obtained to define a cohesive law.

For mode I delamination, a recent study [22] investigated the interlaminar properties of E-glass non-crimp fabric (NCF) reinforced vinylester as described above. The study showed that a cohesive law can be determined through an inverse modelling scheme. In the present paper, the aim is to determine the mixed mode cohesive law for the same NCF composite. Six samples were tested for each of five moment configurations: mode I, mode II and three different mixed modes. The experimental tests are described in Section 3. The mixed mode cohesive law is obtained from the experimental data through inverse modelling using 3D finite element simulation. In

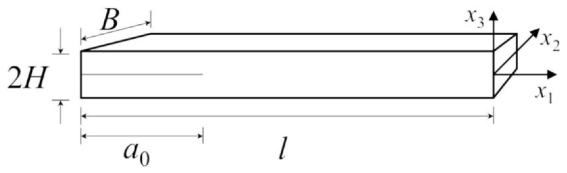

Fig. 1. DCB test specimen geometry.

this way, the variations in crack opening displacement across the specimen are taken into account. The J integral approach is used to find a starting point for the fitting procedure.

2. The path independent J integral approach

The path independent J integral was first applied to crack problems by Rice [20] and can be used to calculate the fracture resistance, J_R.

A simple double cantilever beam (DCB) specimen is illustrated in Fig. 1. Evaluating the J integral along the external boundaries of such a DCB specimen when deformed by bending moments applied to the beam ends as illustrated in Fig. 2(a) gives (assuming plane stress) [16]

$$J_{R,ext} = \frac{21(M_1^2 + M_2^2) - 6M_1M_2}{4B^2H^3E_{11}} \quad |M_1| < M_2 \tag{1}$$

where M_1 and M_2 are the moments applied to the beam ends, B and H are the beam width and height, respectively and E_{11} is the Young's modulus in the x_1-direction.

Evaluating the J integral along the edge of the FPZ in Fig. 2(b) gives [21]

$$J_{R,FPZ} = \int_0^{\delta_n^*} \sigma_n(\delta_n, \delta_t)d\delta_n + \int_0^{\delta_t^*} \sigma_t(\delta_n, \delta_t)d\delta_t \tag{2}$$

where σ_n and σ_t are the local normal and tangential tractions (both being functions of the local normal and tangential separations, δ_n and δ_t) while δ_n^* and δ_t^* are the openings at the end of the FPZ. In Eq. (2), the cohesive laws represent the entire fracture process including the crack tip separation, i.e., the energy J_{tip} associated with the crack tip region Γ_{tip} shown in Fig. 2(b), is embedded in the two integrals via the cohesive law, which is of the form shown in the lower part of Fig. 2(c). The energy associated with the crack tip can also be separated out of Eq. (2), the law would then be referred to as a bridging law, as illustrated in Fig. 2(c) with a much lower peak traction compared to the cohesive law that includes the crack tip. The integrals in Eq. (2) can be understood as the work (per unit area) of the normal and tangential tractions at the end of the FPZ, respectively.

Due to path-independence, $J_{R,ext} = J_{R,FPZ}$. A large portion of the fracture energy $J_{R,FPZ}$ dissipated from crack initiation to total separation is caused by crack tip deformations. This portion of the fracture energy is normally referred to as J_0, and is characterised by small opening displacements and high tractions. When $J_{R,ext}$ exceeds J_0, the dissipated fracture energy is assumed to be caused by fibre bridging. This part of the fracture process is characterised by larger opening displacements and significantly lower tractions. With increasing $J_{R,ext}$, the length of the FPZ, L, and the end-opening, $\delta^* = \sqrt{(\delta_n^*)^2 + (\delta_t^*)^2}$, increase as the crack extends. When δ^* reaches a critical value, J_0, the fracture surfaces are completely separated at the end of the FPZ. The FPZ is then fully developed, and the fracture resistance attains a constant value referred to as the steady-state fracture resistance J_{SS}. The values of J_{SS}, δ_0 and J_0 depend on the opening mode.

For mode I, the relation between the tractions and the opening separation at the crack end can be obtained by differentiating the external J integral with respect to the crack end opening [23,24]. For mixed mode conditions, the cohesive laws for the interface are obtained by partial differentiation [21]:

$$\sigma_n(\delta_n^*, \delta_t^*) = \frac{\partial J_{R,ext}(\delta_n^*, \delta_t^*)}{\partial \delta_n^*} \quad \sigma_t(\delta_n^*, \delta_t^*) = \frac{\partial J_{R,ext}(\delta_n^*, \delta_t^*)}{\partial \delta_t^*} \tag{3}$$

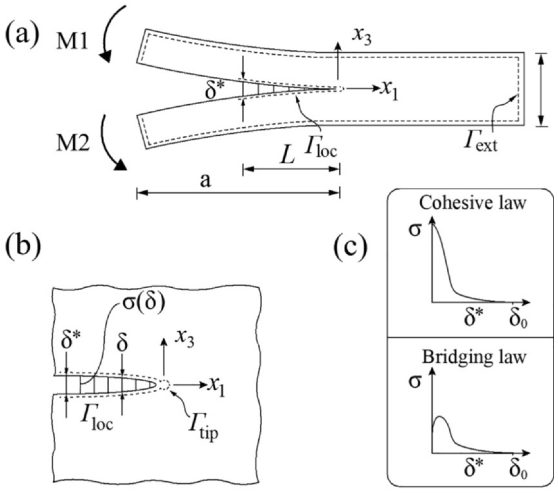

Fig. 2. (a) External and local integration paths Γ_{ext} and Γ_{loc} for the DCB specimen, showing the length L of the fracture process zone (FPZ), (b) enlarged view of the local integration path along the FPZ and (c) a schematic illustration of a bridging law and a cohesive law.

Eq. (3) give the values of the normal and shear tractions at the end of the FPZ, respectively. By analysing the mixed mode experiments for data from zero to steady-state the normal and shear tractions are obtained for all values of δ_n^* and δ_t^*. Assuming that the cohesive laws are the same at all locations within the FPZ, the traction-separation laws obtained using Eq. (3) are thus representative for the entire FPZ.

3. Experimental setup, data analysis and results

The DCB-UBM (double cantilever beam loaded by uneven bending moments) tests were carried out as described by Sørensen et al. [16] on NCF reinforced vinylester. The reinforcement was of the type L 900-E10-F (E-Glass) produced by Devold AMT, and the vinylester was of the type Dion 9102 produced by Reichhold. The material properties and geometric specifications are listed in Table 1. Note that these are laminate properties, not UD-ply properties. This material system was characterised for intra-laminar failure and post-failure behaviour by Joki et al. [25]. The L 900 reinforcement has 5% of the fibres oriented in the transverse direction (the x_2-direction – see Fig. 1). These transverse fibres are called backing fibres and are provided to stabilise the longitudinal fibres during production and subsequent handling. They are not present for mechanical purposes but do affect the mechanical behaviour of the final laminate and therefore need to be considered in the modelling. The reinforcement layers are stacked such that the upper and lower fracture surfaces have fibres oriented in the x_1-direction. A 12-μm PTFE film is inserted at mid-depth in the lay-up during production of the laminates to produce an initial crack of length $a_0 = 60$ mm in the x_1-direction.

Moments were applied to the specimens as illustrated in Fig. 3 by lowering the loading beam under the specimen at a constant rate. The loads P_1 and P_2 were measured using load cells. The distances L_1 and L_2 determine the moments, i.e. $M_1 = L_1P_1$ and $M_2 = L_2P_2$. The moment configuration is in the following referred to as φ which is defined as $\varphi = M_1/M_2$ for $M_2 \geq |M_1|$. Equal moments in opposite directions, i.e. $\varphi = -1$, promote mode I delamination. Mode II delamination is promoted when $\varphi \approx 1$. However, for pure mode II the curvatures of the beams at the FPZ must be equal, whereas the curvatures at the neutral axes of the beams would be equal if the moments were equal. Typically, the maximum moment ratio is 0.99 [19]. Intermediate values promote mixed mode delamination. The five moment configurations chosen in this study were: $\varphi = -1$, 0, 0.299, 0.629 and 0.986.

The specimens were fitted with two LVDTs and an extensometer to measure δ_n^* and δ_t^* as described by Sørensen and Jacobsen [19]. The opening mode angle is defined as $\theta = \tan^{-1}(\delta_t^*/\delta_n^*)$. Acoustic emission sensors were used to detect the onset of crack growth.

The histories of the fracture resistance, calculated from Eq. (1), and the end opening mode angle θ, in terms of their variation with the fracture end opening, are presented in Fig. 4(a) and (b), respectively. Fig. 5(a) illustrates schematically how the fracture initiation energy, J_0, the steady-state fracture resistance, J_{ss}, and the critical crack end opening displacement, δ_0, are obtained from fracture resistance curves such as those in Fig. 4(a). Fig. 5(b), (c) and (d) show how J_0, J_{ss}, and δ_0, respectively, change with the configuration of the applied moments. The observed result from each individual specimen is indicated with triangles and a dashed line is drawn through the average from each moment configuration.

It was found that the fracture resistance curves could conveniently be fitted by exponential decay functions. The opening displacements at which the fitted functions were 98% of the value at the horizontal asymptote were taken as the critical opening displacement. This was not possible for the specimens with $\varphi = 0.986$. As seen in Fig. 4, for these specimens the fracture resistance increased steadily throughout the test. Specimens with all five mode-mixities were investigated by cutting several sections from the delaminated specimens (in the x_2-x_3-plane). Studying the fracture surface in the wake of the crack tip revealed dry fibres covering the fractured surfaces as evidence of fibre bridging. Fig. 6 shows that the extent of fibre bridging varies with the moment configuration. In Fig. 7, where the crack end openings are plotted up to 1.0 mm, it can be seen that the specimens with $\varphi = 0.986$ reached a plateau at approximately 3.7 kJ/m^2. The fracture resistance seems to increase steadily as observed in Fig. 4(a), where the openings are plotted for a larger range of opening displacements. The deformations of cantilever beams calculated for this moment configuration show that the deflection of the beams will make them come in contact and that the contact force will increase with the magnitude of the beam's curvature. Thus, the apparent rise in fracture resistance for these specimens is assumed to be caused by increasing friction. Therefore, the fracture resistance plotted in Fig. 5(c) for the specimens loaded with $\varphi = 0.986$ is the value observed at 0.5 mm crack end opening.

The phase angle of the openings, θ, is a natural parameter for the characterisation of mode mix of cohesive laws. For small scale FPZs (i.e. under LEFM conditions), an alternative to θ is the phase angle of the stress intensity factor, defined as $\psi = \tan^{-1}(K_{II}/K_I)$, where K_I and K_{II}, are the mode I and mode II stress intensity factors respectively. Near the crack tip (within the zone of dominance of

Table 1
Geometric and material properties of the specimens as defined by Joki et al. [22].

B	30.11	mm	Width
$2H$	17.40	mm	Thickness
l	300	mm	Length
a_0	60	mm	Initial delamination length
E_{11}	37	GPa	Longitudinal Young's modulus (laminate)
E_{22}	12	GPa	Transverse Young's modulus (laminate)
ν_{12}	0.29		Poisson's ratio (laminate)
S_{22}	28	MPa	Ply transverse elastic limit
S_{12}	50	MPa	Ply shear elastic limit

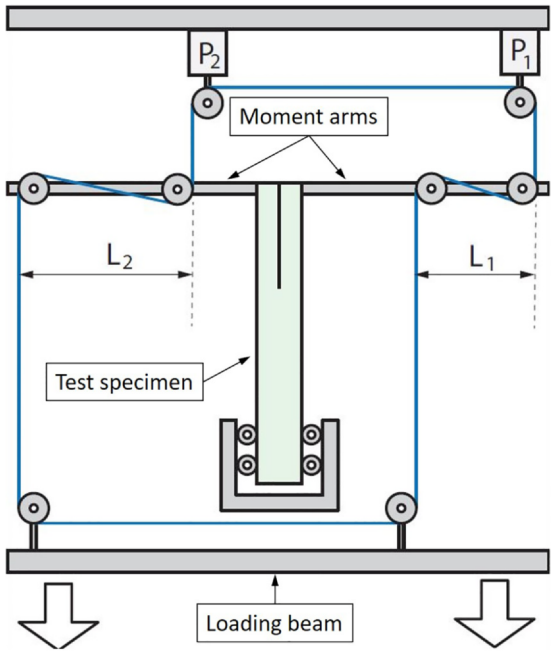

Fig. 3. Schematic illustration of DCB-UBM test fixture with test specimen.

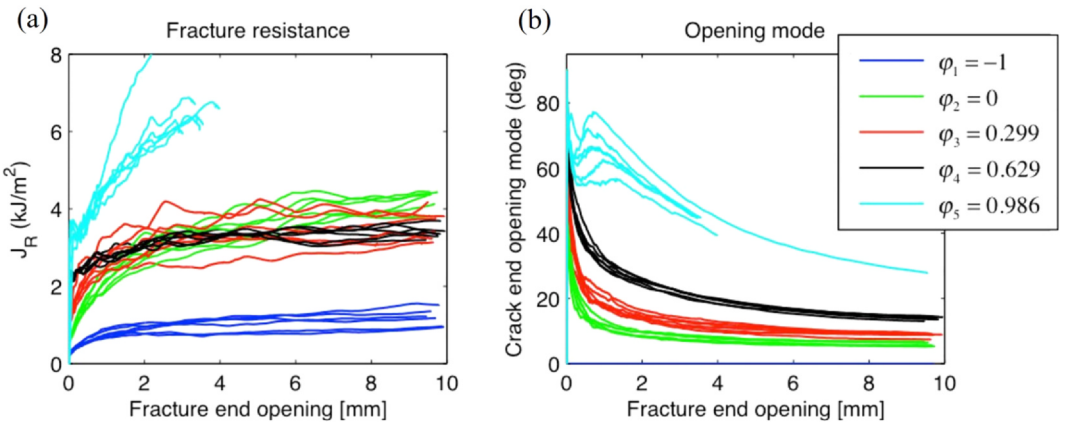

Fig. 4. (a) Fracture resistance, J_R, and (b) corresponding crack end opening mode angle θ. Both fracture resistance and opening mode angle are plotted against the absolute opening displacement measured at the initial crack tip. The legend shows the configurations of the moments applied to the beam ends, represented by the parameter φ.

the K-field), the two mode mix measures are related by $\tan\theta = \lambda^{1/2}\tan\psi$, where $\lambda = E_{22}/E_{11}$ is a non-dimensional elastic parameter [26,27], and $\theta = \psi$ for $\lambda = 1$. The mode mixity ψ can be calculated from the moment configurations as [16]:

$$\psi = \tan^{-1}\left[\lambda^{-1/4}\frac{\sqrt{3}}{2}\left(\frac{M_2 + M_1}{M_2 - M_1}\right)\right]. \tag{4}$$

The reason for using Eq. (4) is that in practice the opening mode angle, θ, cannot be calculated with sufficient accuracy from the measurements for small end-openings, when the opening displacements do not exceed the noise levels of the displacement transducers.

Due to Poisson effects, the stress field in the vicinity of the crack tip will vary across the specimen width [22,28]. At the free edge at each side of the specimen the stress state will approach plane stress whereas at half-width the stress state will have a component in the x_2–direction (see Fig. 1). Due to this difference in the stress field, the crack tip will start to develop at the half-width position, while the opening displacements at the free edges initially remain zero as the fracture resistance rises with increasing applied moments. Then, for small crack openings, the opening displacement measured at the edge of the specimen is not representative for the whole width of the specimen. This effect continues as the crack opens further and the respective parts of the beam develop bending deformations in the transverse direction (anticlastic curvature).

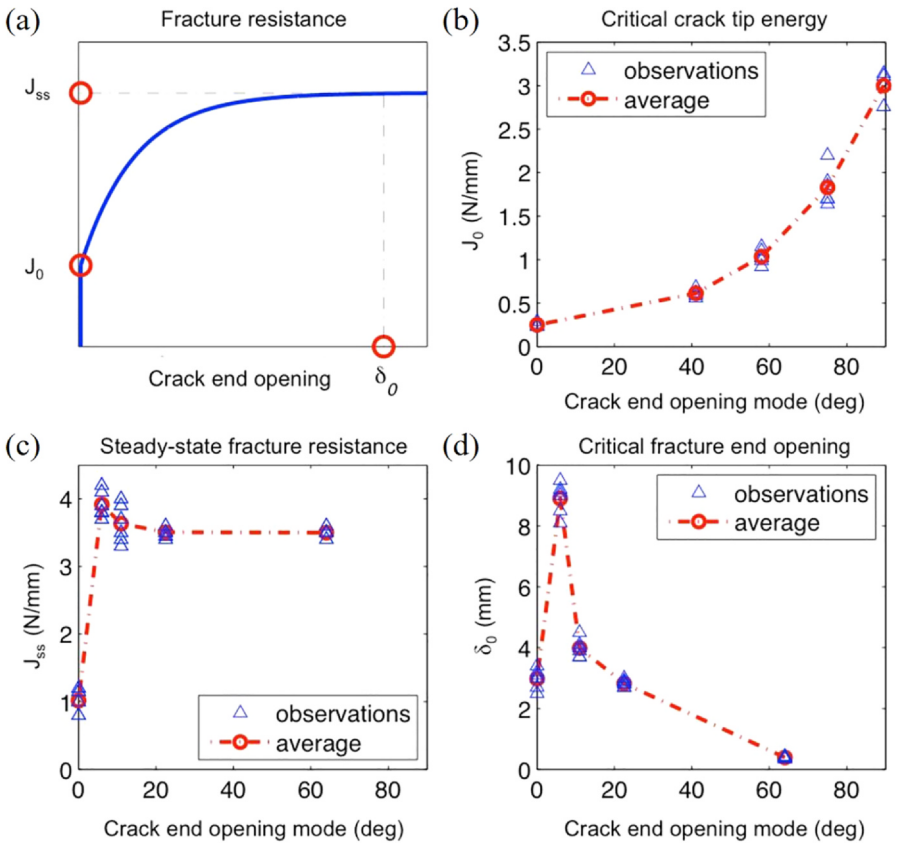

Fig. 5. (a) Key properties of the fracture resistance curve, (b) crack tip energy dissipation vs mode mixity, (c) steady-state fracture resistance as a function of opening mode and (d) effective fracture opening at the end of the fracture process zone (FPZ) vs opening mode.

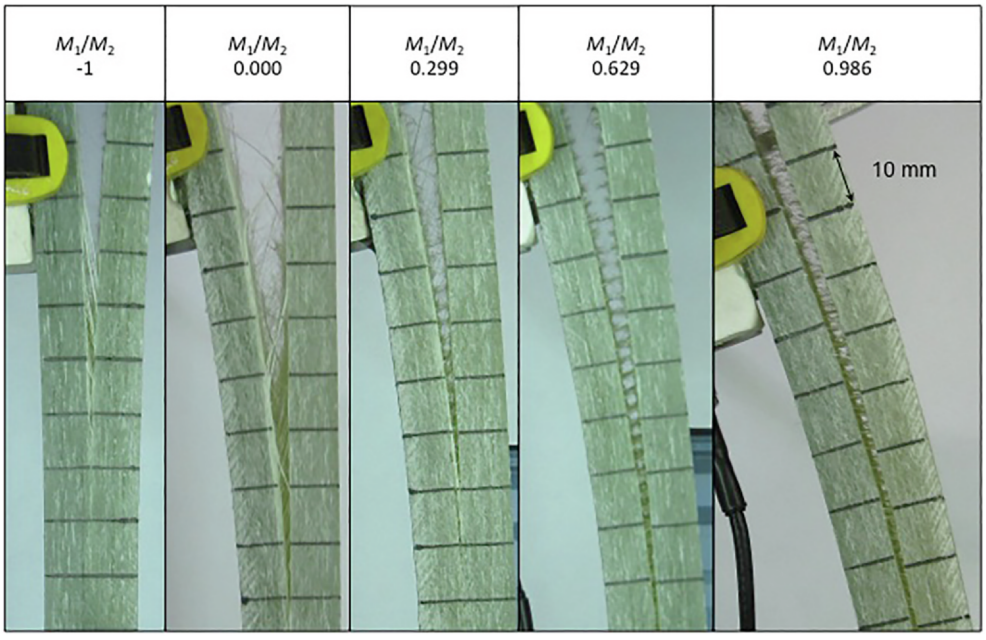

Fig. 6. Test specimens showing that the extent of fibre bridging varies with the moment configuration.

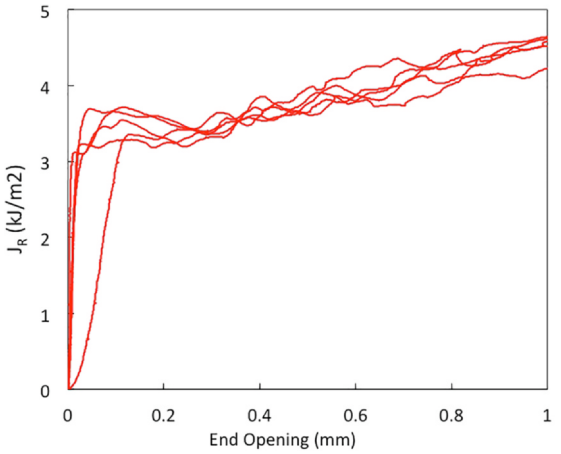

Fig. 7. Fracture resistance, J_R vs. absolute opening displacement measured at the crack end from the specimens loaded with moment configuration $\varphi = 0.986$.

The challenge of determining the critical stresses associated with J_0 can be addressed by investigating the properties of the bulk material. Mode I cohesive tractions should not exceed the tensile strength of the bulk material loaded transversely to the fibre direction. Mode II cohesive tractions should not exceed the shear strength of the bulk material. The limiting values for the transverse and shear stress are given by S_{22} and S_{12}, respectively, in Table 1.

4. The cohesive material model

A user defined cohesive material model is implemented in the LS-DYNA finite element code [10]. To be generally applicable to any engineering problem, the cohesive model must be able to describe both loading and unloading. A damage parameter, D, is therefore introduced and the relation between tractions and separations is given by:

$$\begin{bmatrix}\sigma_1\\ \sigma_2\\ \sigma_3\end{bmatrix} = \begin{bmatrix} k_1(1-D) & 0 & 0\\ 0 & k_2(1-D) & 0\\ 0 & 0 & k_3(1-D)\end{bmatrix}\begin{bmatrix}\delta_1\\ \delta_2\\ \delta_3\end{bmatrix}, \tag{5}$$

where δ_i are the opening separations, σ_i are the tractions and k_i are the corresponding stiffnesses. The numerical subscripts refer to the element coordinate axes where 1 and 2 lie in the plane of the delamination propagation and direction 3 is normal to the delamination propagation, thus $\sigma_n = \sigma_3$, $\sigma_t = \sqrt{\sigma_1^2 + \sigma_2^2}$ and the effective cohesive traction is $\sigma_e = \sqrt{\sigma_n^2 + \sigma_t^2}$. The cohesive opening separations in Eq. (5) are the separations of the element centres at the upper and lower cohesive element surfaces. The fracture opening separations are related to the element separations by $\delta_n = \delta_3$ and $\delta_t = \sqrt{\delta_1^2 + \delta_2^2}$. The stiffness relating the tractions to the separation is given by $k_i = \sigma_i^0/\delta_i^0$, where σ_i^0 and δ_i^0 are the traction and separation, respectively, at the end of the linear traction-separation relation. The damage parameter, D, does not affect the traction-separation relation during crack closure, as described by the following relations

$$\begin{aligned}\sigma_n &= \begin{cases}(1-D)\bar{\sigma}_n, & \bar{\sigma}_n \geqslant 0\\ \bar{\sigma}_n, & \bar{\sigma}_n < 0\end{cases}\\ \sigma_t &= (1-D)\bar{\sigma}_t\ ,\end{aligned} \tag{6}$$

where σ_n and σ_t are tractions from a cohesive law and the tractions indicated with a bar are fictitious tractions calculated from k_i and the current separation assuming linear elasticity. The damage parameter D is initially zero but is updated in every load step j

Table 2
Tabulated mixed mode cohesive law for opening displacement, $\delta_{e,lm}$, at opening mode angle θ_m.

	$\theta_1 = 0^\circ$		$\theta_2 = 6^\circ$		$\theta_3 = 22.5^\circ$		$\theta_4 = 58^\circ$		$\theta_5 = 90^\circ$	
l	$\delta_{e,l1}$ [mm]	$\sigma_{e,l1}$ [MPa]	$\delta_{e,l2}$ [mm]	$\sigma_{e,l2}$ [MPa]	$\delta_{e,l3}$ [mm]	$\sigma_{e,l3}$ [MPa]	$\delta_{e,l4}$ [mm]	$\sigma_{e,l4}$ [MPa]	$\delta_{e,l5}$ [mm]	$\sigma_{e,l5}$ [MPa]
1	0.0000	0.0000	0.0000	0.0000	0.0000	0.0000	0.0000	0.0000	0.0000	0.0000
2	0.0010	20.0000	0.0010	20.6155	0.0011	22.3082	0.0013	25.9500	0.0023	45.0000
3	0.0151	20.0000	0.0169	20.6155	0.0191	22.3082	0.0347	25.9500	0.0477	45.0000
4	0.0181	0.6200	0.0203	1.0660	0.0229	2.0816	0.0416	1.6089	0.0572	0.6975
5	1.5088	0.1568	4.4500	0.2696	2.0145	0.5264	1.2508	0.4069	0.2529	0.1764
6	3.0176	0.0000	8.9000	0.0000	4.0291	0.0000	2.5016	0.0000	0.5057	0.0000

according to

$$D_j = \max\left(D_{j-1},\ 1 - \frac{\sigma_{e,j}}{\bar{\sigma}_{e,j}}\right). \tag{7}$$

The damage parameter D is included so that unloading and non-proportional loading (changing mode mixity) can be described in a more realistic way. Note that D is path dependent and causes the tractions to be dependent on all opening components. The normal and tangential constitutive tractions at load step i, $\sigma_{n,i}$ and $\sigma_{t,i}$ are calculated from the normal and tangential components of $\sigma_{e,i}$ according to Eq. (6).

With only a scalar damage parameter, the cohesive law is described by a single surface in the domain of effective traction $\sigma_e = \sqrt{\sigma_n^2 + \sigma_t^2}$, effective opening separation $\delta_e = \sqrt{\delta_n^2 + \delta_t^2}$ and opening mode angle $\theta = \tan^{-1}(\delta_n/\delta_t)$, as $\sigma_e = \Omega(\delta_e, \theta)$. The surface Ω is given by linear interpolation (in the domain of δ_e and θ) between values at a selection of grid-points obtained by inverse modelling. The grid points are given for five different opening mode angles: mode I, mode II, and three mixed mode angles. The values of the three mixed mode angles are chosen to best describe the characteristics presented in Fig. 5(c) and (d). The values of the mixed mode cohesive law parameters obtained by the optimisation process described below are presented in Table 2 and illustrated in Fig. 8.

5. Determining the mixed cohesive law

The mixed mode cohesive law is defined by the surface $\sigma_e = \Omega(\delta_e, \theta)$. This is used for the determination of the damage parameter D as described in Eq. (7). The value of $\Omega(\delta_e, \theta)$ has been determined from a series of six opening displacements (represented by suffices $l = 1,2,3,4,5,6$) and five opening mode angles (represented by suffices $m = 1,2,3,4,5$) as shown in Table 2. These define a total of 30 points on the surface. The complete surface is defined by linear interpolation between these 30 values (in the domain of δ_e and θ).

First, the results from Section 3 are investigated in order to determine approximate values for $\sigma_{e,lm}$. In the second step, a full 3D FE model of the DCB-UBM specimen is prepared. In the third step, the approximate values of $\sigma_{e,lm}$ are fitted through inverse modelling [29] using LS-DYNA in combination with the optimisation tool LS-OPT [30] with the experimental results as objective for the optimisation. In the fourth and final step, the accuracy of the fitted cohesive law is evaluated by modelling standardised delamination tests on the same laminates described in Section 3.

5.1. Determining approximate values for the cohesive law

The cohesive law needs to describe two distinctly different phenomena: 1) crack tip deformation and 2) fibre bridging. As noted earlier, the crack tip deformations are associated with small opening displacements and high traction values, whereas fibre bridging is associated with larger opening displacements and low tractions. The effective opening displacements $\delta_{e,1m}$, $\delta_{e,2m}$ and $\delta_{e,3m}$ are assigned to describe crack tip deformations, and $\delta_{e,4m}$, $\delta_{e,5m}$ and $\delta_{e,6m}$ represent predominantly fibre bridging deformations.

5.1.1. Crack tip

For all mode mixities $\delta_{e,1m} = 0$ and $\Omega(\delta_{e,1m}, \theta_m) = 0$, where l represents the opening displacement sequence and m the opening mode angle sequence as described earlier. As discussed in Section 3, the experimental results suggest that J_0 is dissipated over a small, near-zero opening displacement. Therefore, the critical crack tip energy J_0 needs to be dissipated over the opening displacement defined by $\delta_{e,3m}$. Thus the integral of $\Omega(\delta_e, \theta_m)$ from $\delta_{e,1m}$ to $\delta_{e,3m}$ at a given opening mode angle θ_l should equal J_0 as presented in

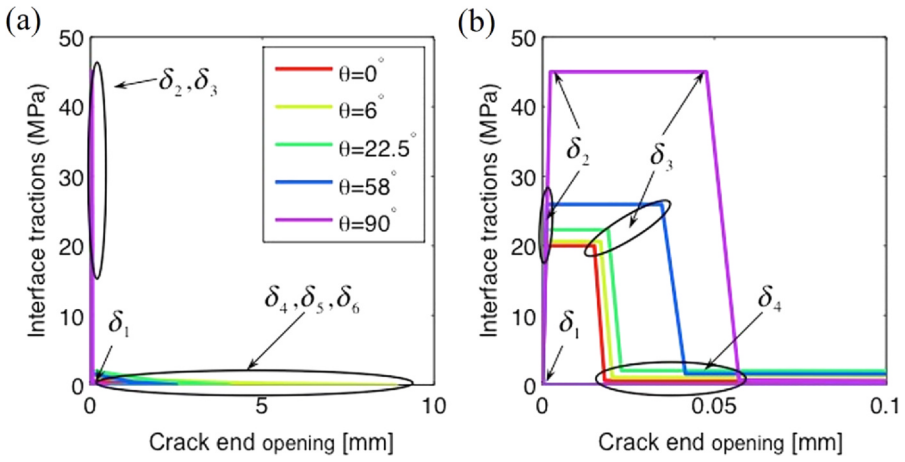

Fig. 8. (a) The calculated cohesive laws plotted with effective tractions vs effective opening displacements, and (b) a close-up of the crack tip part of the same cohesive laws.

Fig. 5(a) for the specified mode angle.

The dissipation of J_0 over a near-zero displacement is addressed by making the following assumptions: 1) the cohesive stiffness of the finite-thickness element should resemble the stiffness of the bulk material, and 2) the cohesive traction should not exceed that of the bulk material. The choice of $\delta_{e,2m}$ is thus constrained by the cohesive stiffnesses k_i and the value of $\sigma_{e,2m}$. In order to dissipate J_0 over the shortest possible opening displacement, $\sigma_{e,3m}$ should equal $\sigma_{e,2m}$. This is then the critical cohesive traction for the mode mixity defined by θ_m.

If the change in J_0 from mode I to mode II is caused by the characteristics of the specific failure process, it is reasonable to assume that the critical traction level associated with the failure process changes in a similar manner. The critical tractions in mode I, $\sigma_{e,21}$ and $\sigma_{e,31}$ ($\theta_1 = 0^\circ$), and mode II, $\sigma_{e,25}$ and $\sigma_{e,35}$ ($\theta_5 = 90^\circ$) are therefore given by S_{22} and S_{12}, respectively, in Table 1, and the change in critical traction from mode I to mode II is fitted to follow the evolution of J_0.

5.1.2. Fibre bridging

All the fracture resistance curves presented in Fig. 4(a) have a rapid reduction in slope when the crack tip energy is reached. The rapid reduction in slope demands a significantly reduced cohesive traction within a small increase in opening displacement between $\delta_{e,3m}$ and $\delta_{e,4m}$, where the suffix m refers to the opening mode angle, θ_m. The cohesive tractions should therefore be given at closely separated opening values. The opening displacement $\delta_{e,4m}$ is therefore fixed at $\delta_{e,4m} = 1.25\delta_{e,3m}$. This choice presents a limitation to the optimisation procedure but will reduce the number of variables and thus the computational cost. The slopes of the fracture resistance curves observed in Fig. 4(a) cannot be used directly. The estimated value of $\Omega(\delta_{e,4m}, \theta_m)$ for the first iteration in the fitting procedure is therefore set arbitrarily to 5% of the critical cohesive tractions at $\Omega(\delta_{e,4m}, \theta_m)$ and subsequently kept as a variable for the optimisation process.

The opening displacement $\delta_{e,5m}$ is fixed at half the opening displacement at the steady-state fracture resistance, i.e. $\delta_{e,5m} = 0.5\delta_{e,6m}$. The effective cohesive traction at $\Omega(\delta_{e,5m}, \theta_m)$ is fixed at 25% of $\Omega(\delta_{e,4m}, \theta_m)$. In this way the fitting of $\Omega(\delta_{e,4m}, \theta_m)$ will also adjust the value of $\Omega(\delta_{e,5m}, \theta_m)$ while keeping the ratio between them constant. In the fitting procedure this saves significant computational costs.

The cohesive law should prescribe zero traction at openings larger than the critical separations ($\delta > \delta_0$). The effective opening displacement should then be as presented in Fig. 5(d), which is given by the opening at the initial crack tip when the fracture resistance reaches a steady state, J_{ss}, as illustrated in Fig. 5(a). This gives $\Omega(\delta_{e,6m}, \theta_m) = 0$, and $\delta_{e,6m}$ can be approximated for any values of θ_m by assuming linear interpolation between the measured values presented in Fig. 5(d).

The only opening displacement that is set as a variable to be optimised is that governing the dissipated crack tip energy, $\delta_{e,4m}$. The other opening variables are determined based on the assumptions made above. The effective cohesive tractions $\Omega(\delta_{e,4m}, \theta_m)$ are set as variables to be optimised in the fitting procedure. The rest are determined based on the assumptions made above. In total there are 10 independent variables (five opening displacements and five tractions), 10 dependent variables (five opening displacements and five tractions) and 40 constants including the zero tractions at zero opening displacements and steady-state fracture resistance.

The cohesive stiffnesses, k_i, from Eq. (5) are determined based on the thickness of the cohesive element and elastic properties of the bulk material.

5.1.3. Fitting procedure

The FE model used in the fitting procedure is presented in Fig. 9. The simulation uses implicit time integration with adaptive time

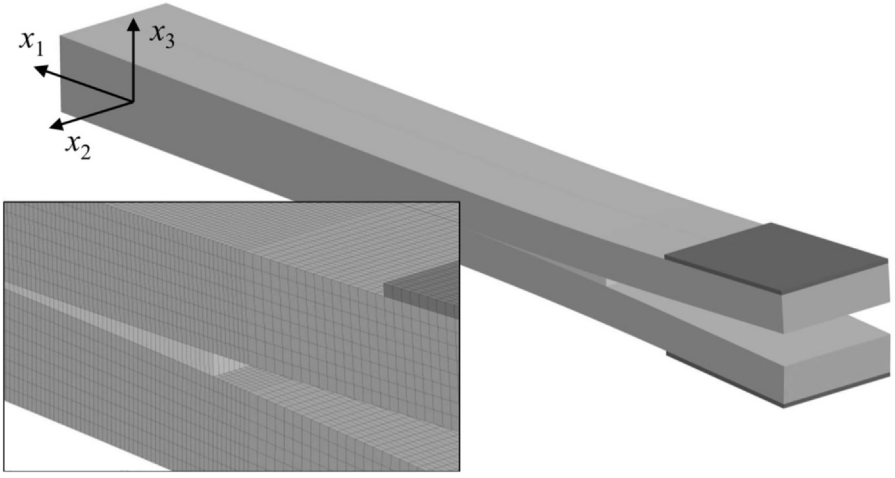

Fig. 9. The FEM model of the DCB-UBM specimen. Monotonically increasing moments are applied to rigid bodies, the surfaces shown in darker grey at the beam ends. The modelled ridged bodies do not represent the geometry of the metal fixtures applied to the beams. The metal fixtures have a thickness of approximately 1.2 × H and they are both bolted and adhesively bonded to the beams. A rigid body representation of the fixtures will not have a significant effect on the behaviour of the beams.

stepping to ensure convergence. Because the tractions transferred between the two fracturing surfaces fall to extremely low values as the fracturing surfaces move apart, the tolerance for the displacement norm was set to 10^{-10} (the default value is 10^{-3}) and the tolerance for the energy norm was set to 10^{-7} (default 10^{-3}) to reduce the jaggedness in the simulated opening-displacement curve at the initial crack tip. These tolerance values were established by trial and error.

Numerical delamination models are known to be mesh size dependent if coarse meshes are used [31]; the element size should be chosen to be sufficiently small so that the results are not mesh dependent. In this model the element dimensions in the plane of delamination were 0.5 mm × 0.5 mm, i.e. 30 square elements across the modelled width of half the specimen. The fully developed FPZ in mode I simulation was more than 40 mm long and thus covered by more than 80 cohesive elements in the direction of crack propagation. The evolution of the crack tip, i.e. the development of J_0, was covered by approximately 5–10 elements as the crack propagated. The actual number of elements that cover the complete FPZ depends on the shape of the cohesive law. It is important to adjust the loading step size in the analysis so that the separation parameters describing the development of J_0 are captured.

The optimisation process in LS-OPT is based on the response surface methodology [32]. The aim is to minimize the residual between a response from the model and a response from experimental test results. The relation between crack tip opening displacements and applied moments recorded from the experiments is used as objective for the optimization process. An adaptive simulated annealing (ASA) hybrid optimisation scheme [30] with a D-optimal sampling procedure of linear order is used [30]. The optimisation procedure is an iterative process where each iteration requires a minimum number of sampling points. Each sampling point is a calculated residual between a response from the model and a response from experimental test results. The effective crack tip opening as a function of applied moments is the response used to find the residual between model and experiment in this study. Every sampling point therefore represents a complete FEM simulation of the delamination test. The minimum number of sampling points, p, is given by $p = 1.5(n + 1) + 1$, where n is the number of variables [30]. It was therefore desirable to limit the numbers of variables. Data from all five moment configurations tested experimentally were used in the optimisation process. The optimisation procedure is schematically illustrated in the flow-chart presented in Fig. 10.

The fitted mixed mode cohesive law is assessed by comparing numerical simulations with a separate set of experimental results, namely the ASTM D 6671 Mixed Mode Bending (MMB) test [33] and the ASTM D 5528 Double Cantilever Beam (DCB) test [34]. The

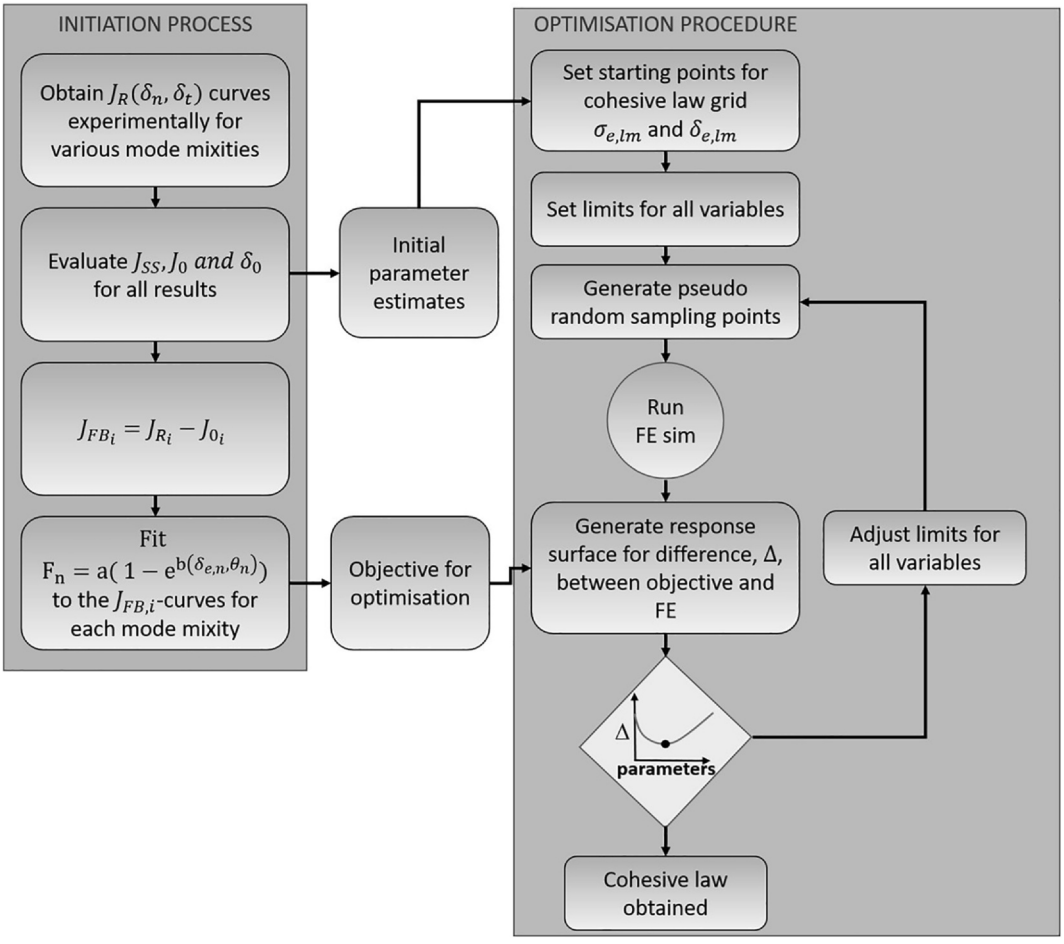

Fig. 10. Flowchart representing the optimisation procedure used to obtain the cohesive law.

specimens used in these standardised tests were produced with the same material system and curing procedure as the specimens used in the DCB-UBM tests. They had the dimensions $B = 10$ mm, $2H = 4$ mm, $l = 100$ mm and $a_0 = 25$ mm (see geometry in Fig. 1). With the identified mixed mode cohesive laws, the FE model was used for modelling the MMB test specimen illustrated in Fig. 11 (the same model with the same dimensions except that the loading fixture is used for simulating the DCB test). Again, implicit time integration with adaptive time steps is applied.

6. Results

The experimental results presented in Section 3 show a rising fracture resistance with increasing opening displacement. The fracture resistance reaches a steady-state value for all moment configurations except mode II. The steady-state value, J_{ss}, for all mixed mode moment configurations seems to take approximately the same value around 3.5–4 kJ/m^2, see Fig. 4(a).

For mode II ($\varphi = 0.986$) the fracture resistance appears to keep rising continuously with increasing crack end opening displacement. The observable extent of fibre bridging is shown in Fig. 6. Closer examination of the fracture resistance curve showed a flat region starting at an approximate opening displacement of 0.2–0.5 mm (see Fig. 7). From crack end opening displacements of 0.5–0.7 mm the curves started to rise again. It was not possible to determine whether friction and/or fibre bridging caused this continuous increase of the fracture resistance with increasing crack end opening, but a plausible explanation in terms of increasing friction between the deforming beam portions has been presented in Section 3.

The observed behaviour of the critical crack tip energy J_0 shows a clear mode mixity dependence. J_0 increased from an average value of 0.25 kJ/m^2 in mode I, to 3.00 kJ/m^2 in mode II. The fracture resistance response from the optimisation process is presented in Figs. 12–15. The resulting effective traction values defining the cohesive law are presented in Table 2.

The implemented cohesive model manages to reproduce the difference in evolution of critical crack tip energy, steady-state fracture resistance and critical end opening in the mixed mode DCB-UBM tests with acceptable accuracy. The opening mode angle is predicted well by the mixed mode test with moment configuration $\varphi = 0.000$, acceptably for $\varphi = 0.299$ but not as well for $\varphi = 0.629$. One possible explanation for the discrepancy between model and experiment for this case is that the crack tip associated with mode II opening displacement deforms plastically and that local permanent deformations force the beams apart. Such effects are not included in the FE-model. The opening displacement paths were not included in the optimisation process.

The numerical results from simulation of the ASTM standardised Mixed Mode Bending (MMB) delamination tests were compared with corresponding experimental test results in Fig. 16 in order to assess the accuracy of the proposed approach. The two MMB tests are equal except for the load-offset distance c (see Fig. 11) measured from the point at which the downward loading is applied, midway between the lower supports. In Fig. 16(a), $c = 60$ mm, the experimental results have a load–displacement relationship that is linear up to a displacement of approximately 5 mm, with a peak load at 130 N. The FEM result shows linear load–displacement behaviour up to approximately 6 mm, and a peak load at 155 N. This gives an error of 25 N (16%). In Fig. 16(b), $c = 117$ mm, the experimental load–displacement linearity ends at a displacement of approximately 4 mm, and the peak load is 45 N. The FEM result shows linear load–displacement behaviour up to approximately 3 mm, and has a peak load at 55 N. This gives an error of 10 N (18%). Here the curve from FEM shows some oscillations, indicating some numerical instability. In Fig. 16(c), DCB – mode I, the experimental load–displacement relationship is linear up to a displacement of approximately 6 mm, and the peak load is 38 N. The FEM result shows linear load–displacement behaviour up to approximately 7.5 mm, and a peak load at 40 N. This gives an error of 2 N (5%).

7. Discussion

As mentioned above, the fracture resistances observed in Fig. 4 are a result of two distinct phenomena: the energy dissipation at the creation of new fracture surfaces at the crack tip, and the work of the tractions created by the fibre bridging in the wake of the crack. Since the fracture specimens all had a thin film acting as a crack starter, the J_0 values shown in Fig. 5(b) are associated with the

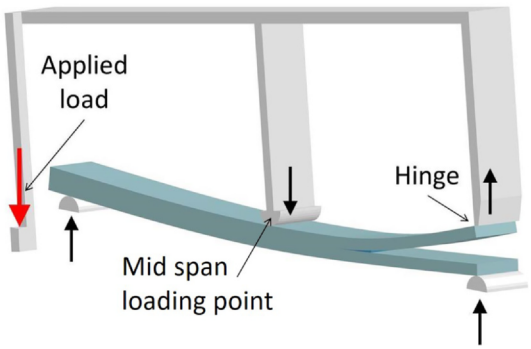

Fig. 11. FEM model of the ASTM D 6671 Mixed Mode Bending test. The DCB specimen and the loading fixture is modelled with a symmetry plane along the half width of the specimen. The longitudinal distance between the loading point and the midspan of the specimen is denoted c in the results.

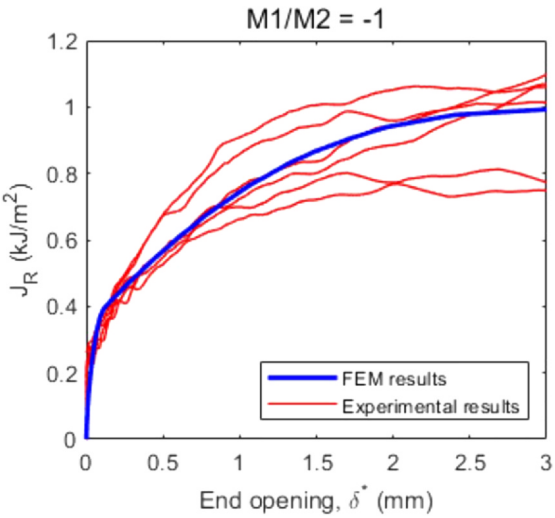

Fig. 12. Fracture resistance J_R vs effective end opening displacement from FEM and experimental results for $M_1/M_2 = -1$.

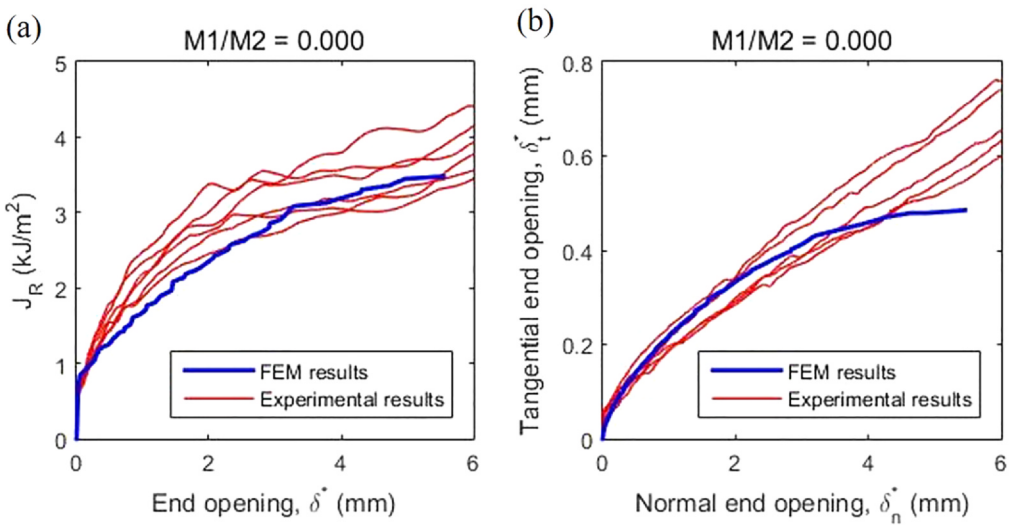

Fig. 13. Fracture resistance J_R vs effective end opening displacement on the left side and normal vs. tangential opening displacement on the right side, from FEM and experimental results for $M_1/M_2 = -0.000$.

onset of cracking with no fibre bridging and the increase from J_0 to J_{ss} is attributed primarily to fibre bridging. The change in the steady-state fracture resistance with mode mixity, $J_{SS}(\theta)$, as observed in the experimental results presented in Fig. 5(c), can be explained by the evolution of these two phenomena.

The energy dissipated in the wake of the crack tip is caused by the work of the cohesive tractions transmitted across the crack faces by intact fibres. This mechanism is controlled by fibre–matrix debonding and fibre failure [17,35]. The fibres that are bridging between the two surfaces in mode I delamination are exposed to a different loading scenario at their ends from the bridging fibres in mode II delamination. A micromechanical model of mixed mode crack bridging by intact fibres [36] predicts that, with other parameters fixed, the fracture resistance under mode II will be higher than that under mode I. Furthermore, the model predicts that for mode I, the fracture resistance should increase proportionally to the square root of the end-opening, whereas for mode II the fracture resistance should increase linearly with the tangential opening displacement.

The work presented in this paper demonstrates that it is crucial to consider the effects of the full stress field when characterising cohesive laws from mechanical test results. However, two aspects of this study need continued work efforts: (1) The evaluation of the Mode II ($\varphi = 0.986$) test results clearly needs to be further investigated. The contribution from fibre bridging to the fracture resistance is likely higher for this delamination mode than that indicated in this paper. The presented work demonstrates the need for the optimisation procedure for determining a cohesive law regardless of these limitations. (2) A sensitivity study on the effects of the variables, starting conditions and boundaries set for the optimisation procedure would also be beneficial to the quality of the presented approach to characterise cohesive laws.

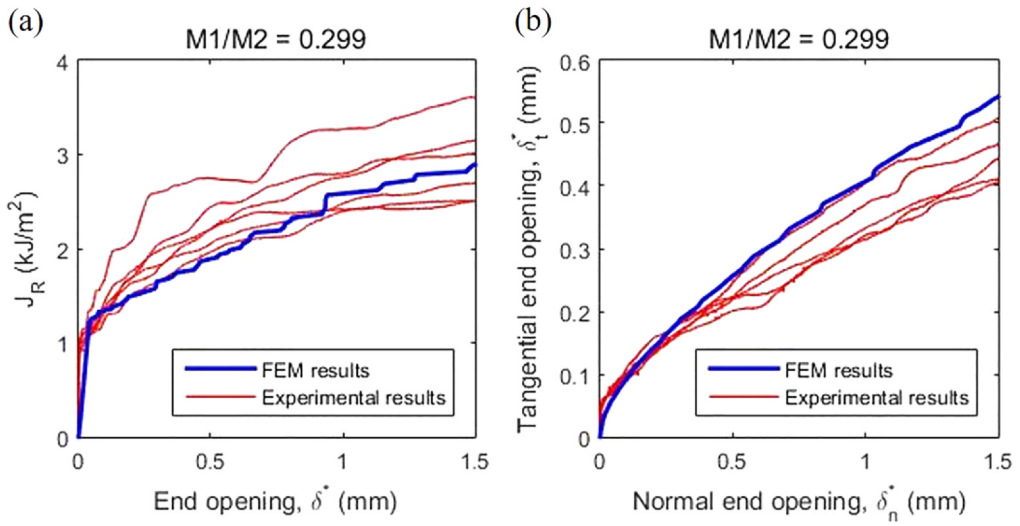

Fig. 14. Fracture resistance J_R vs effective end opening displacement on the left side and normal vs. tangential opening displacement on the right side from FEM and experimental results for $M_1/M_2 = -0.299$.

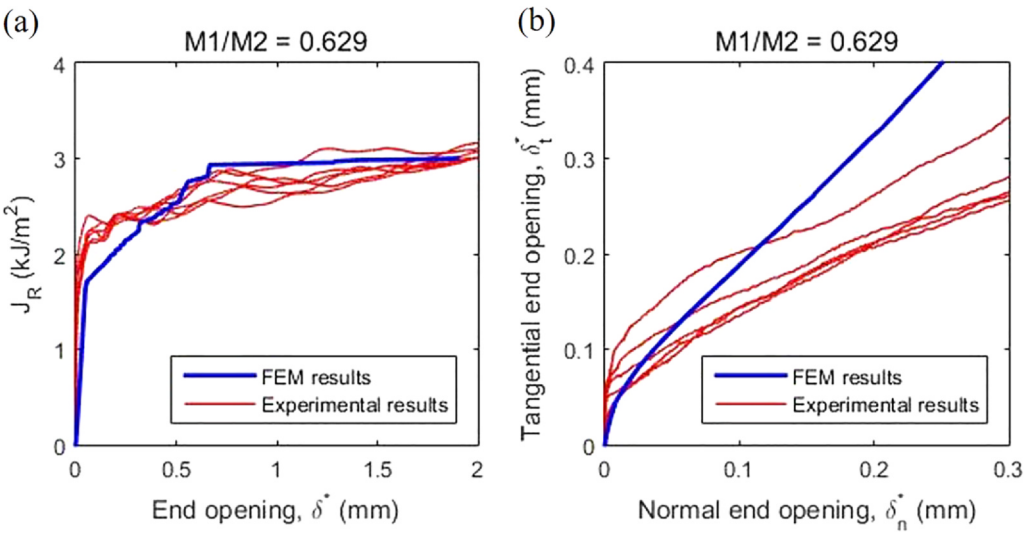

Fig. 15. Fracture resistance J_R vs effective end opening displacement on the left side and normal vs. tangential opening displacement on the right side from FEM and experimental results for $M_1/M_2 = -0.629$.

8. Conclusions

A mixed mode cohesive law has been defined in the domain of effective cohesive traction, effective opening displacement and opening mode angle. The law was implemented in the FE code LS-DYNA.

The agreement between model prediction and experimental results gives some confidence in the approach for cohesive law determination, since the mixed mode cohesive laws were obtained independently by DCB-UBM tests. Understanding that the cohesive law needs to describe both crack tip and fibre bridging, and that these two distinct phenomena are different with respect to the scale of tractions and opening displacements, made it possible to produce acceptable results with a relatively simple cohesive law.

Declaration of Competing Interest

The authors declare that they have no known competing financial interests or personal relationships that could have appeared to influence the work reported in this paper.

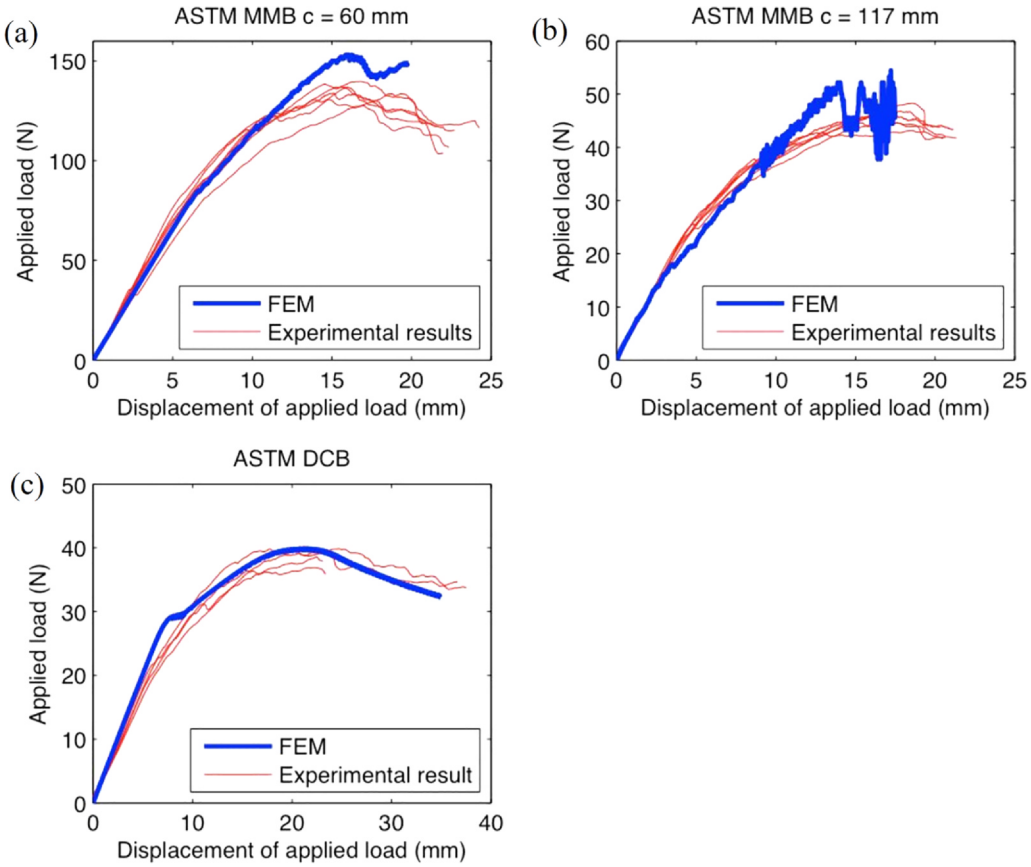

Fig. 16. Model testing by comparing standardised experimental test results and FEM results for (a) MMB with c = 60 mm, (b) MMB with c = 117 mm and (c) from the mode I loaded DCB.

Acknowledgements

This work was part of the collaborative project "Composite structures under impact loading" with the industrial partners Flowtite Technology AS, Nammo Raufoss AS, Ragasco AS and the research institutes Norwegian University of Science and Technology (NTNU), University of Oslo (UiO), SINTEF Materials and Chemistry and SINTEF Raufoss Manufacturing. The authors would like to express their thanks for the financial support by the Norwegian Research Council (grant 193238/i40), Norwegian Research Centre for Offshore Wind Technology (NOWITECH) and industrial partners, and finally for the financial support by the European Council through the H2020 project DACOMAT (grant 761072). The fourth author was supported by the Danish Centre for Composite Structures and Materials for Wind Turbines (DCCSM), grant no. 09-067212 from the Danish Strategic Research Council.

References

[1] Dantuluri V, Maiti S, Geubelle PH, Patel R, Kilic H. Cohesive modeling of delamination in Z-pin reinforced composite laminates. Compos. Sci. Technol. 2007;67(3–4):616–31. https://doi.org/10.1016/j.compscitech.2006.07.024.
[2] Xie D, Salvi AG, Sun C, Waas AM, Caliskan A. Discrete cohesive zone model to simulate static fracture in 2D triaxially braided carbon fiber composites. J. Compos. Mater. 2006;40(22):2025–46. https://doi.org/10.1177/0021998306061320.
[3] Camanho PP, Davila CG, de Moura MF. Numerical simulation of mixed-mode progressive delamination in composite materials. J. Compos. Mater. 2003;37(16):1415–38. https://doi.org/10.1177/0021998303034505.
[4] Tvergaard V. Effect of fibre debonding in a whisker-reinforced metal. Mater. Sci. Eng. A 1990;125(2):203–13. https://doi.org/10.1016/0921-5093(90)90170-8.
[5] Blackman B, Hadavinia H, Kinloch A, Williams J. The use of a cohesive zone model to study the fracture of fibre composites and adhesively-bonded joints. Int. J. Fract. 2003;119(1):25–46.
[6] Xu X, Needleman A. Void nucleation by inclusion debonding in a crystal matrix. Model. Simul. Mater. Sci. Eng. 1993;1(2):111–32. https://doi.org/10.1088/0965-0393/1/2/001.
[7] van den Bosch MJ, Schreurs PJG, Geers MGD. An improved description of the exponential Xu and Needleman cohesive zone law for mixed-mode decohesion. Eng. Fract. Mech. 2006;73(9):1220–34. https://doi.org/10.1016/j.engfracmech.2005.12.006.
[8] Tvergaard V, Hutchinson JW. The relation between crack growth resistance and fracture process parameters in elastic-plastic solids. J. Mech. Phys. Solids 1992;40(6):1377–97. https://doi.org/10.1016/0022-5096(92)90020-3.
[9] Yang Q, Cox B. Cohesive models for damage evolution in laminated composites. Int. J. Fract. 2005;133(2):107–37. https://doi.org/10.1007/s10704-005-4729-6.
[10] "LS-DYNA Keyword User's Manuals Version 971, Livermore Software Technology Corporation." 2007.
[11] Benzeggagh ML, Kenane M. Measurement of mixed-mode delamination fracture toughness of unidirectional glass/epoxy composites with mixed-mode bending

apparatus. Compos. Sci. Technol. 1996;56(4):439–49. https://doi.org/10.1016/0266-3538(96)00005-x.
[12] Campilho RDSG, Banea MD, Neto JABP, da Silva LFM. Modelling adhesive joints with cohesive zone models: effect of the cohesive law shape of the adhesive layer. Int. J. Adhes. Adhes. 2013;44:48–56. https://doi.org/10.1016/j.ijadhadh.2013.02.006.
[13] Sills RB, Thouless MD. The effect of cohesive-law parameters on mixed-mode fracture. Eng. Fract. Mech. 2013;109:353–68. https://doi.org/10.1016/j.engfracmech.2012.06.006.
[14] Scheider I, Hachez F, Brocks W. Effect of cohesive law and triaxiality dependence of cohesive parameters in ductile tearing. In: Fracture of nano and engineering materials and structures. Netherlands: Springer; p. 965–66, doi: 10.1007/1-4020-4972-2_478.
[15] Li S, Thouless MD, Waas AM, Schroeder JA, Zavattieri PD. Use of mode-I cohesive-zone models to describe the fracture of an adhesively-bonded polymer-matrix composite. Compos. Sci. Technol. 2005;65(2):281–93. https://doi.org/10.1016/j.compscitech.2004.07.009.
[16] Sørensen BF, Jørgensen K, Jacobsen TK, Østergaard RC. DCB-specimen loaded with uneven bending moments. Int. J. Fract. 2006;141(1–2):163–76. https://doi.org/10.1007/s10704-006-0071-x.
[17] Sørensen BF, Jacobsen TK. Determination of cohesive laws by the J integral approach. Eng. Fract. Mech. 2003;70(14):1841–58. https://doi.org/10.1016/s0013-7944(03)00127-9.
[18] Olsson P, Stigh U. On the determination of the constitutive properties of thin interphase layers - an exact inverse solution. Int. J. Fract. 1989:71–6.
[19] Sørensen BF, Jacobsen TK. Characterizing delamination of fibre composites by mixed mode cohesive laws. Compos. Sci. Technol. 2009;69(3–4):445–56. https://doi.org/10.1016/j.compscitech.2008.11.025.
[20] Rice JR. A path independent integral and the approximate analysis of strain concentration by notches and cracks. J. Appl. Mech. 1968;35(2):379–86. https://doi.org/10.1115/1.3601206.
[21] Sørensen BF, Kirkegaard P. Determination of mixed mode cohesive laws. Eng. Fract. Mech. 2006;73(17):2642–61. https://doi.org/10.1016/j.engfracmech.2006.04.006.
[22] Joki RK, Grytten F, Hayman B, Sørensen BF. Determination of a cohesive law for delamination modelling - Accounting for variation in crack opening and stress state across the test specimen width. Compos. Sci. Technol. 2016;128. https://doi.org/10.1016/j.compscitech.2016.01.026.
[23] VC L, RJ W. A novel testing technique for post-peak tensile behaviour of cementitious materials. In: H M, H T, FH W, editors. Fracture toughness and fracture energy – testing methods for concrete and rocks. Rotterdam: A.A. Balkema Publishers; 1989, p. 183–95.
[24] Suo Z, Bao G, Fan B. Delamination R-curve phenomena due to damage. J. Mech. Phys. Solids 1992;40(1):1–16. https://doi.org/10.1016/0022-5096(92)90198-b.
[25] Joki RK, Grytten F, Hayman B. Nonlinear response in glass fibre non-crimp fabric reinforced vinylester composites. Compos. Part B Eng. 2015;77. https://doi.org/10.1016/j.compositesb.2015.03.001.
[26] Suo Z, Bao G, Fan B, Wang TC. Orthotropy rescaling and implications for fracture in composites. Int. J. Solids Struct. 1991;28(2):235–48. https://doi.org/10.1016/0020-7683(91)90208-w.
[27] Sun J, Deng Z, Li Z, Tu M. Stress triaxiality in crack tip regions of bend specimens with different crack-depth and fracture criterion at initiation. Eng. Fract. Mech. 1990;36(2):321–6. https://doi.org/10.1016/0013-7944(90)90011-5.
[28] Kotousov A, Lazzarin P, Berto F, Harding S. Effect of the thickness on elastic deformation and quasi-brittle fracture of plate components. Eng. Fract. Mech. 2010;77(11):1665–81. https://doi.org/10.1016/j.engfracmech.2010.04.008.
[29] Tarantola A. Inverse problem theory and methods for model parameter estimation. Society for Industrial and Applied Mathematics; 2005.
[30] LS-OPT User's Manual Version 4.2 LIVERMORE SOFTWARE TECHNOLOGY CORPORATION; 2012.
[31] Turon A, Dávila CG, Camanho PP, Costa J. An engineering solution for mesh size effects in the simulation of delamination using cohesive zone models. Eng. Fract. Mech. 2007;74(10):1665–82. https://doi.org/10.1016/j.engfracmech.2006.08.025.
[32] Gunst RF, Myers RH, Montgomery DC. Response surface methodology: process and product optimization using designed experiments. Technometrics 1996;38(3):285. https://doi.org/10.2307/1270613.
[33] ASTM D 6671 Standard Test Method for Mixed Mode I-Mode II Interlaminar Fracture Toughness of Unidirectional Fiber Reinforced Polymer Matrix Composites; 2009.
[34] ASTM D 5528 Standard Test Method for Mode I Interlaminar Fracture Toughness of Unidirectional Fiber-Reinforced Polymer Matrix Composites; 2009.
[35] Spearing SM, Evans AG. The role of fiber bridging in the delamination resistance of fiber-reinforced composites. Acta Metall. Mater. 1992;40(9):2191–9. https://doi.org/10.1016/0956-7151(92)90137-4.
[36] Sørensen BF, Gamstedt EK, Østergaard RC, Goutianos S. Micromechanical model of cross-over fibre bridging – Prediction of mixed mode bridging laws. Mech. Mater. 2008;40(4–5):220–34. https://doi.org/10.1016/j.mechmat.2007.07.007.